Journal of Power Sources 196 (2011) 8352–8359

Contents lists available at ScienceDirect

Journal of Power Sources

journal homepage: www.elsevier.com/locate/jpowsour

Performance of double-perovskite $Sr_{2-x}Sm_xMgMoO_{6-\delta}$ as solid-oxide fuel-cell anodes

Leilei Zhang [a,b], Tianmin He [a,*]

[a] State Key Laboratory of Superhard Materials, College of Physics, Jilin University, Changchun, 130012, PR China
[b] College of Sciences, Liaoning University of Petroleum and Chemical Technology, Fushun, 113001, PR China

ARTICLE INFO

Article history:
Received 26 April 2011
Received in revised form 16 June 2011
Accepted 17 June 2011
Available online 24 June 2011

Keywords:
Solid oxide fuel cell
Anode
Electrical conductivity
Cell fabrication
Electrochemical performance
City gas

ABSTRACT

Double-perovskite $Sr_{2-x}Sm_xMgMoO_{6-\delta}$ (SSMM, $0 \le x \le 0.8$) is investigated as a possible anode material for solid-oxide fuel cells on $La_{0.9}Sr_{0.1}Ga_{0.8}Mg_{0.2}O_{3-\delta}$ (LSGM) electrolytes. Single-phase SSMM samples with $0 \le x \le 0.4$ are prepared. At $x \ge 0.6$, a small amount of $SrMoO_4$ and Sm_2O_3 impurities are observed. The Mg/Mo ordering in SSMM decreases with increasing Sm content. Substitution of Sm for Sr significantly improves the electrical conductivity of SSMM. At $x = 0.6$, the sample yields the highest conductivity, with values reaching 16 S cm^{-1} in H_2 at 800 °C. The maximum power densities of single cells achieved with $x = 0.0$, 0.2, 0.4, 0.6, and 0.8 anodes on a 300 μm-thick LSGM electrolyte are 693, 770, 860, 907, and 672 mW cm^{-2}, respectively, in H_2 at 850 °C. The SSMM sample with $x = 0.4$ is considered as the best anode candidate because of the impurity formation seen in $x \ge 0.6$ samples. The $x = 0.4$ sample not only has a thermal-expansion coefficient closer to that of the LSGM electrolyte but also exhibits good electrochemical performance and stability in commercial city gas containing H_2S, where the maximum power density achieved is 726 mW cm^{-2} at 850 °C.

1. Introduction

Solid-oxide fuel cells (SOFCs) are electrochemical devices used for the direct conversion of a fuel into electrical power with high efficiency, low cost, and little pollution [1]. A significant advantage of SOFCs lies in the high flexibility of fuel choice, which allows direct utilization of hydrocarbon fuels without any pretreatment [2–5]. Therefore, development of anode materials for SOFCs that operate directly on low-cost and more-abundant hydrocarbon fuels, such as natural gas, has attracted considerable interest over the last few years [2,6–8]. Conventional nickel/electrolyte composite anodes show good performance using pure H_2 as fuel. However, such anodes also have some disadvantages, such as poor redox stability, carbon deposition, sulfur poisoning when used on natural gas, and the tendency of Ni particles to agglomerate after prolonged operation [9]. Aside from doped-$SrTiO_3$ mixed ionic and electronic conductors (MIECs) [10,11], other MIECs that have been investigated as potential anode materials over the last few years include $Ln_{1-x}Sr_xCr_{0.5}Mn_{0.5}O_{3-\delta}$ (Ln = La and Pr) [6,12,13], $La_4Sr_8Ti_{11}Mn_{0.5}Ga_{0.5}O_{37.5-\delta}$ [14–16], $Ce_{0.9}Sr_{0.1}VO_x$ ($x = 3$, 4) [17], $Ca(V_{0.5}Mo_{0.5})O_3$ [18], and $Sr_2Fe_{4/3}Mo_{2/3}O_6$ perovskites [19]. Chromium–manganites have exhibited performances comparable with those of nickel/zirconia cermets in H_2 and excellent catalytic activity for the electro-oxidation of CH_4 at high temperature [20]. However, these manganites exhibit low electronic conductivity at reduced atmospheres (~1 S cm^{-1} at 1000 °C) and low tolerance against sulfur species in the fuel [21]. Titanates have shown high redox and chemical stability and high resistance to poisoning by sulfur impurities, but their electrocatalytic activity and ionic conductivity require further improvement [14].

Double-perovskite $Sr_2MgMoO_{6-\delta}$ (SMM) has recently been developed by Huang et al. [22,23] as an efficient SOFC anode operating on natural-gas fuel. This material shows high redox stability, good sulfur tolerance, excellent electrochemical performance, and sufficient electron conductivity. The presence of oxygen vacancies in this sample not only yields good oxide-ion conduction but also creates mixed-valent $Mo^{5+/6+}$ species, hence, significantly improving electronic conduction [22–24]. Modification of SMM by the substitution of La for Sr to enhance single-cell performance in natural-gas and high-carbon fuels was reported by Ji et al. [25]. However, these substituted SMM phases are unstable in oxidation atmospheres because of phase segregations above 600 °C, which impose a severe limitation on the fabrication of SOFCs [26]. In addition, re-oxidation of these pre-reduced samples at high temperature in oxidation atmosphere could lead to a marked decrease in oxygen-vacancy concentration. To ensure the formation of

* Corresponding author. Tel.: +86 431 85166112; fax: +86 431 85166112.
E-mail addresses: hetm@jlu.edu.cn, hly@mail.jlu.edu.cn (T. He).

0378-7753/$ – see front matter © 2011 Elsevier B.V. All rights reserved.
doi:10.1016/j.jpowsour.2011.06.064

oxygen vacancies in SMM, Huang et al. [22,23] reduced the sample in 5% H_2/Ar at 800 °C for 20 h before the cell test. Marrero-López et al. [27] and Bernuy-Lopez et al. [28] also confirmed the formation of oxygen vacancies in SMM samples to a limited extent even under a strongly reduced atmosphere.

In the current paper, with the aim of preventing phase segregations and enhancing oxygen-vacancy concentration, a single cell is fabricated in a nitrogen atmosphere, and the properties of double-perovskite $Sr_{2-x}Sm_xMgMoO_{6-\delta}$ (SSMM, $0 \le x \le 0.8$) are systematically investigated as SOFC anodes. In addition, with $La_{0.9}Sr_{0.1}Ga_{0.8}Mg_{0.2}O_{3-\delta}$ (LSGM) as the electrolyte, $SmBaCo_2O_{5+x}$ (SBCO) as the cathode, and SSMM as the anodes, the electrochemical performance of a single cell in H_2 and commercial city gas containing H_2S was tested.

2. Experimental setup

2.1. Sample preparation

The SSMM samples ($0 \le x \le 0.8$) were synthesized by a sol–gel technique using citric acid as the chelating agent and $Sr(NO_3)_2$, $Sm(NO_3)_3$, $Mg(NO_3)\cdot 6H_2O$, and $(NH_4)_6Mo_7O_{24}\cdot 4H_2O$ as the starting materials. The gel was first decomposed at 400 °C in air for 6 h and subsequently calcined at 800 °C in air for 10 h. The calcined powder was pelletized and subsequently sintered at 1200 °C in a flowing atmosphere of 5% H_2/Ar for 20 h with an intermediate ground. The double-perovskite cathode SBCO was synthesized by a solid-state reaction described earlier [29]. The LSGM and $Ce_{0.8}Sm_{0.2}O_{1.9}$ (SDC) electrolytes were obtained from a glycine–nitrate process [30,31].

2.2. Characterization

The electrical conductivity of the SSMM samples was measured in H_2 by the van der Pauw method using a standard DC voltage/current generator and a precision digital multimeter, as described in Ref. [32]. Before measurement, the sample was reduced in H_2 at 850 °C for 2 h.

A single cell was fabricated by an electrolyte-supported technique with 300 μm-thick LSGM as the electrolyte, SBCO as the cathode, and SSMM as the anodes. A thin SDC interlayer was added between the SSMM anodes and the LSGM electrolyte to prevent interdiffusion of ionic species and was sintered at 1300 °C for 1 h. The anodes were screen painted onto the interlayer and subsequently sintered at 1100 °C for 1 h [33]. The SBCO cathode was painted onto the opposite side of the electrolyte by screen printing and sintered at 950 °C for 2 h. Both the anodes and the cathode were sintered in a nitrogen atmosphere to prevent phase segregations and re-oxidation of the SSMM anodes. Single-cell performance was determined using an electrochemical analyzer (CHI604C) using H_2 and commercial city gas containing H_2S as the fuels and ambient air as the oxidant. The phase purity and crystalline structure of the samples were examined using an X-ray diffractometer (Rigaku-D-Max γA, Cu Kα, λ = 0.15418 nm) at room temperature by step scanning in the angle range of 15–85° with increments of 0.02°. The unit-cell parameters were derived from a computerized least square refinement technique using the CELREF program. A Raman spectrometer (Renishaw inVia), equipped with an argon-ion laser operating at an excitation wavelength of 514.5 nm, was also used to analyze the phase compositions and structures of the samples. A scanning electron microscope [(SEM), Hitachi, S-570] was used to inspect the microstructure of the anode surface and the anode/electrolyte interface after cell testing. The thermal-expansion coefficient (TEC) of the samples was measured using a dilatometer (Netzsch DIL 402C) over the temperature range of 30–1000 °C at a heating rate of 5 °C min^{-1} in nitrogen atmosphere with a flow rate of 60 mL min^{-1}.

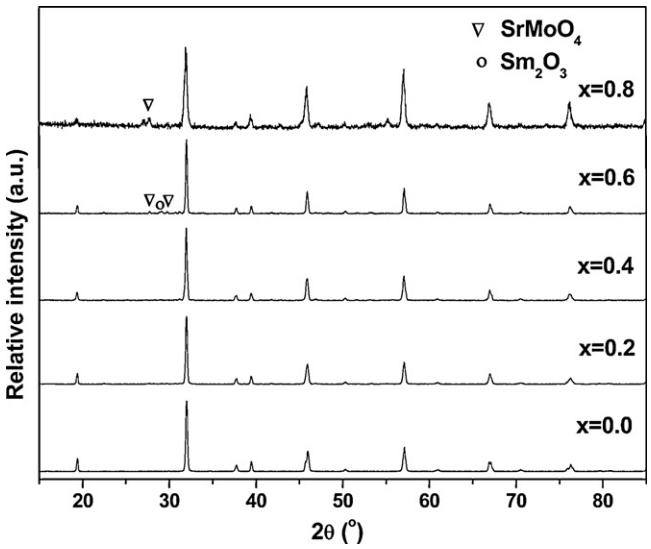

Fig. 1. XRD patterns of the SSMM samples ($0 \le x \le 0.8$) sintered at 1200 °C for 20 h.

3. Results and discussion

3.1. Phase composition, crystalline structure, and stability

Fig. 1 shows the X-ray diffraction (XRD) patterns of double-perovskite SSMM ($0 \le x \le 0.8$) sintered at 1200 °C in 5% H_2/Ar. Pure single-phase SSMM samples with $0 \le x \le 0.4$ are readily achieved. Additional diffraction peaks are observed in the XRD patterns of SSMM samples with $x \ge 0.6$, confirming the formation of a small amount of $SrMoO_4$ and Sm_2O_3 impurities. The crystalline structure of the SSMM ($x = 0.0$) sample was reported to be tetragonal (s.g. $I4/m$) [26], monoclinic (s.g. $P21/n$) [23,25], cubic (s.g. $Fm\bar{3}m$) [34–36], and/or triclinic (s.g. $I\bar{1}$) [26–28]. However, no appreciable differences were observed in the Rietveld refinements from the XRD data when the samples were refined in a triclinic or a tetragonal cell [26].

The ordered double-perovskite $A_2BB'O_{6-\delta}$ has alternating $BO_{6/2}$ and $B'O_{6/2}$ corner-shared octahedra. However, the formation of antisite defects (*i.e.*, the concentration of B ions at the B′ sites) is inevitable. The development of a long-range statistical order in B/B′ cation sites can be monitored by XRD tracing of the super-lattice reflections [37]. Fig. 1 shows that the most relevant trend is the systematic decrease of the diffracted intensity ratio $I_{19.3}/I_{32}$ with increasing Sm^{3+} content, the corresponding values of which are listed in Table 1. The peak at around 19.3° is found to be a super-lattice line, which reflects the ordering of B/B′ ions [37]. Thus, the results shown in Fig. 1 and Table 1 clearly suggest that Sm doping greatly decreases the Mg/Mo ordering. Similar results have also been observed in the $Sr_{2-x}La_xFeMoO_{6-\delta}$ [38] and $Sr_{2-x}La_xMgMoO_{6-\delta}$ [25] samples.

Table 1
Relative diffracted intensity ratio $I(101)/\{I(200)+I(112)\}$.

Composition	$I(101)/\{I(200)+I(112)\}$
$Sr_2MgMoO_{6-\delta}$	0.183
$Sr_{1.8}Sm_{0.2}MgMoO_{6-\delta}$	0.155
$Sr_{1.6}Sm_{0.4}MgMoO_{6-\delta}$	0.114
$Sr_{1.4}Sm_{0.6}MgMoO_{6-\delta}$	0.103
$Sr_{1.2}Sm_{0.8}MgMoO_{6-\delta}$	0.074

Table 2
Unit-cell parameters of SSMM ($0 \le x \le 0.8$) oxides for the space group $I4/m$.

Composition	a (Å)	c (Å)	V (Å^3)
$Sr_2MgMoO_{6-\delta}$	5.574(4)	7.931(4)	246.46
$Sr_{1.8}Sm_{0.2}MgMoO_{6-\delta}$	5.582(6)	7.931(5)	246.63
$Sr_{1.6}Sm_{0.4}MgMoO_{6-\delta}$	5.583(4)	7.922(1)	246.96
$Sr_{1.4}Sm_{0.6}MgMoO_{6-\delta}$	5.584(4)	7.914(3)	246.81
$Sr_{1.2}Sm_{0.8}MgMoO_{6-\delta}$	5.584(5)	7.916(7)	246.88

In the present work, the calculation of parameters for the SSMM ($0 \le x \le 0.8$) oxides at room temperature was performed in tetragonal $I4/m$ models [26], and the unit-cell parameters are listed in Table 2. These results are consistent with those reported by others [23,26–28]. The radii of Sm^{3+} and Sr^{2+} in XII-coordination are 0.124 and 0.144 nm, respectively [39]. The cell volume decreases when Sr^{2+} is replaced by Sm^{3+} in the SSMM. However, in the SSMM ($0 \le x \le 0.4$) system, the replacement of the larger Sr^{2+} by the smaller Sm^{3+} does not decrease the cell volume but increases it. This could be attributed to the decrease in the valence state of Mo from Mo^{6+} to Mo^{5+} (0.059 nm for Mo^{6+} and 0.061 nm for Mo^{5+} in VI-coordination [39]) during the replacement of Sm^{3+} for Sr^{2+}, thus resulting in a decrease of the cell volume. A similar result was also reported in a study of La-doped SMM materials [24].

The micro-Raman technique is useful for analyzing the microstructure and phase compositions of ceramic samples. As mentioned above, the ordered SSMM oxides can also be taken as cubic $Fm\bar{3}m$ structures [34–36]. Group-theory analysis shows that the double-perovskites with B/B′ ordered arrangements have four Raman active modes at room temperature: A_{1g}, E_g, $F_{2g}(2)$, and $F_{2g}(1)$ [35,36]. Fig. 2 shows the Raman spectra of the SSMM samples ($0 \le x \le 0.6$) at room temperature. The two strong peaks at around

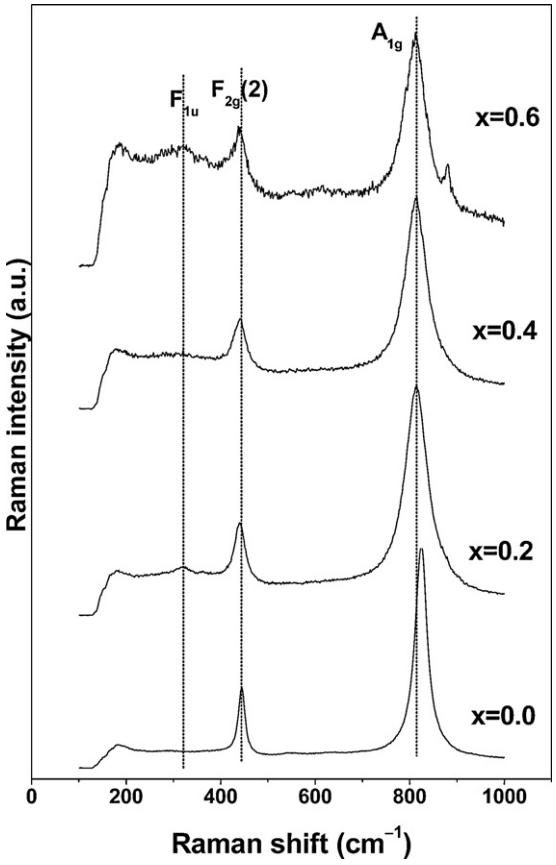

Fig. 2. Raman spectra of the SSMM samples ($0 \le x \le 0.6$) at room temperature.

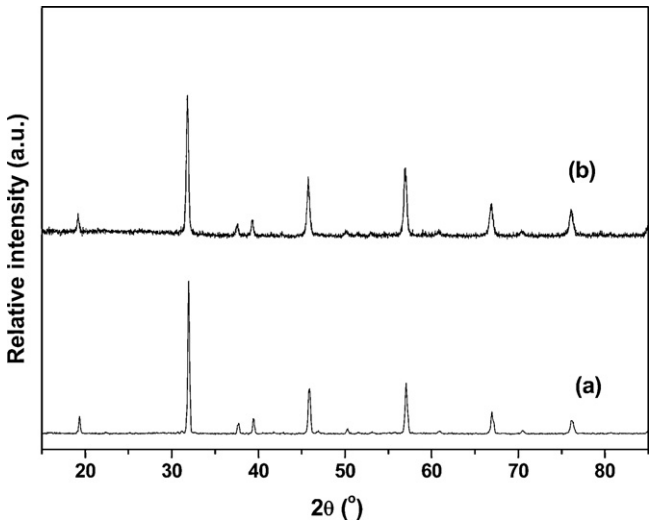

Fig. 3. XRD patterns of the SSMM sample with $x = 0.4$ (a) before and (b) after annealing at 1100 °C for 2 h in a nitrogen atmosphere.

815 and 444 cm^{-1} can be assigned to the Raman active modes of A_{1g} and $F_{2g}(2)$ species, respectively. However, no peaks corresponding to E_g and $F_{2g}(1)$ modes are observed. In the Raman spectra, a weak peak appears at around 320 cm^{-1} as the Sm content increases from $x = 0.2$ to $x = 0.6$. This could be attributed to the F_{1u} mode. According to an earlier work by Ratheesh et al., the appearance of the weak peak could be interpreted as a deviation from cubic symmetry [35]. In the Raman spectrum of SSMM ($x = 0.6$), a weak and sharp peak at 880 cm^{-1} is also observed, which can be identified as the strongest line in the Raman scattering spectrum of the impurity phase of $SrMoO_4$, according to Porto and Scott [40]. These authors showed that the most intense Raman peak of $SrMoO_4$ corresponds to the stretching A_g vibration of MoO_4 group and appeared at around 888 cm^{-1}. Thus, the Raman spectra also confirm that the impurity phase of $SrMoO_4$ appears in the $x \ge 0.6$ samples. This result agrees well with the XRD analysis.

Raman spectra can also be used as analytical tools for tracing the ordering of B/B′ sites in double-perovskites of the type $A_2BB'O_{6-\delta}$. The characteristics of the F_{2g} mode at 444 cm^{-1} are considered to be a key factor in determining the degree of ordering in double-

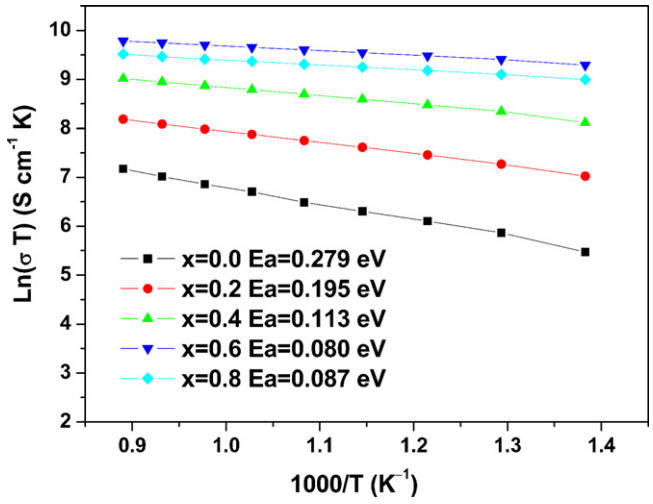

Fig. 4. Temperature-dependence of electrical conductivity of the SSMM sample ($0 \le x \le 0.8$) sintered at 1200 °C for 20 h.

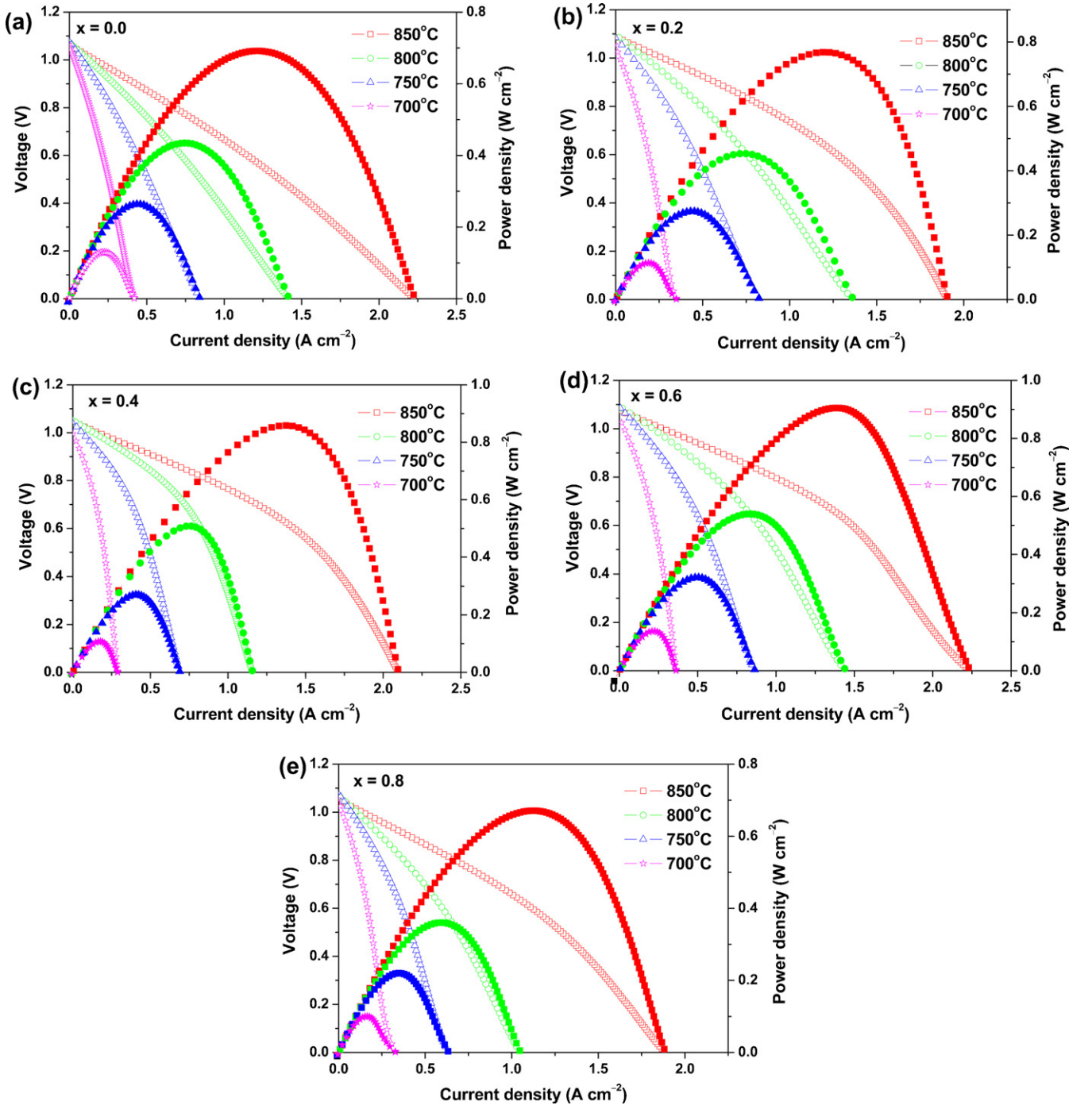

Fig. 5. Cell voltage and power density of SBCO/LSGM/SDC/SSMM cells as functions of current density measured at 700–850 °C using dry H_2 as the fuel and ambient air as the oxidant. (a) $x = 0.0$. (b) $x = 0.2$. (c) $x = 0.4$. (d) $x = 0.6$. (e) $x = 0.8$.

perovskites [35,36]. It should be noted that the line width, rather than the total intensity or the peak frequency, should be taken as the "Raman-order parameter." Fig. 2 shows that the line width of the $F_{2g}(2)$ mode at 444 cm^{-1} increases with increasing Sm content. This observation suggests that the order of the B/B′ sites decreases with the substitution of Sm^{3+} for Sr^{2+}. Clearly, the Raman analysis is consistent with the above XRD result.

The phase stability of the SSMM in a nitrogen atmosphere was examined by annealing at 1100 °C in flowing nitrogen. Fig. 3 shows the XRD patterns of the SSMM sample ($x = 0.4$) before and after annealing at 1100 °C for 2 h in a nitrogen atmosphere. No additional diffraction peaks associated with the impurity phase are observed in the XRD pattern of the sample after annealing, indicating that the SSMM ($x = 0.4$) possesses excellent phase stability at high temperature in a nitrogen atmosphere.

3.2. Electrical conductivity

The electrical conductivity of the SSMM samples ($0 \le x \le 0.8$) was measured by the van der Pauw method at different temperatures in H_2. The Arrhenius plots of the electrical conductivity of the SSMM samples in H_2, measured during the cooling run, are shown in Fig. 4. All the SSMM samples exhibit polaronic conducting behavior in H_2. The electrical conductivity of SMM is only 1 S cm^{-1}

at 800 °C in H_2, which is in good agreement with the result reported by Marrero-López et al. [27,33]. The electrical-conductivity of the SMM sample in the present work is obviously lower than that reported by Huang et al. [22,23] in which the conductivity was 8.6 S cm^{-1} at 800 °C in H_2. This could be explained by the different synthesis conditions employed [27] and the fact that conductivity depends strongly on the reduced state of the sample. Huang et al. [23] reported that the SMM sample prepared in 5% H_2/Ar without further reduction shows very low conductivity (~10^{-2} S cm^{-1} at 800 °C); however, the conductivity increased by almost three orders of magnitude after the sample was further reduced in 5% H_2/Ar for 20 h. The samples in the present work are only reduced in H_2 for 2 h at 850 °C, thus displaying low conductivities. Fig. 4 shows that the conductivity of the samples increases significantly with the substitution of Sm for Sr. The electrical conductivity achieved by the SSMM sample with $x = 0.6$ is 16 S cm^{-1} in H_2 at 800 °C. The substitution of Sm for Sr leads to the partial reduction of Mo^{6+} to Mo^{5+} ions, which produces electronic charge carriers, thus resulting in good electronic conduction. However, the conductivity of the samples decreases with further increases in Sm content when $x > 0.6$. As discussed above, the electronic conduction in perovskite takes place through electron hopping between oxygen ions and Mo^{5+}/Mo^{6+} cations, *i.e.* along the Mo^{5+}–O^{2-}–Mo^{6+} networks. The appearance of the impurity phase inevitably reduces the effective contact area of the SSMM phases and the content of the Mo^{5+}/Mo^{6+} cations and gives rise to an adverse influence on the Mo^{5+}–O^{2-}–Mo^{6+} networks, thus reducing electrical conductivity.

Electronic conduction is carried out through an electron-hopping conduction mechanism between Mo^{6+} and Mo^{5+}. Provided that there is full oxygen stoichiometry ($\delta = 0$) in the SSMM oxides, the amount of the Mo^{5+}/Mo^{6+} redox couple would reach the maximum value at $x = 0.5$ [24,27]. Thus, the electrical conductivity should also show the maximum value at $x = 0.5$. In the present work, the maximum electrical conductivity is achieved at $x = 0.6$, which agrees very well with the analysis discussed above. The activation energy E_a can be obtained from the slopes of the Arrhenius plots of $\ln(\sigma T)$ versus $1/T$, and the E_a values are shown in Fig. 4. E_a gradually decreases with increasing Sm content and achieves a minimum value of 0.080 eV at $x = 0.6$. The amount of Mo^{5+}/Mo^{6+} redox couple is low at $x \leq 0.2$, *i.e.*, there exists only a small amount of electronic charge carriers, leading to a larger E_a [34]. The amount of Mo^{5+}/Mo^{6+} redox couple increases with increasing Sm content from $x = 0.0$ to $x = 0.6$; thus, the E_a decreases. As discussed above, the amount of Mo^{5+}/Mo^{6+} redox couple decreases when $x > 0.6$, resulting in a slight increase in E_a.

3.3. Single-cell performance and SEM

To examine the performance of SSMM as the anode materials of SOFCs, single-cell performances using SSMM anodes were tested using dry H_2 as the fuel and ambient air as the oxidant. Fig. 5 shows the cell voltage and the power density of a typical single-cell with SSMM ($0 \leq x \leq 0.8$) anodes as functions of current density in the temperature range of 700–850 °C in dry H_2. Before testing, the cells were exposed to the fuel gas at 850 °C for 2 h to ensure the formation of oxygen vacancies in the SSMM samples. At 850 °C, the maximum power densities achieved by the cell are 693, 770, 860, 907, and 672 mW cm^{-2} for $x = 0.0$, 0.2, 0.4, 0.6, and 0.8 anodes, respectively. The electrocatalytic activity of double-pervoskite SSMM increases with increasing Sm content, attains a maximum at $x = 0.6$, and subsequently decreases with further increases of x. This result is consistent with the electrical-conductivity results described earlier. As discussed in Section 3.2, the electrical conductivity of SSMM oxides is closely related to the amount of Mo^{5+}/Mo^{6+} redox couples, suggesting that the Mo^{5+}/Mo^{6+} redox couple plays an important role in the electrochemical performance of a cell [22,23]. The ability of Mo^{+6} and Mo^{+5} to form molybdyl ions can reduce two Mo^{6+} to Mo^{5+} by accepting two electrons and create an accompanying oxygen-vacancy formation. This ability is the basis of the catalytic activity of SSMM anodes [8]. In addition, the open-circuit voltage (OCV) values measured are slightly lower than the Nernst values. This is mainly due to the slight gas leaks in the single-cell test. Therefore, the OCV and the cell performance could be further improved by modifying the cell seal.

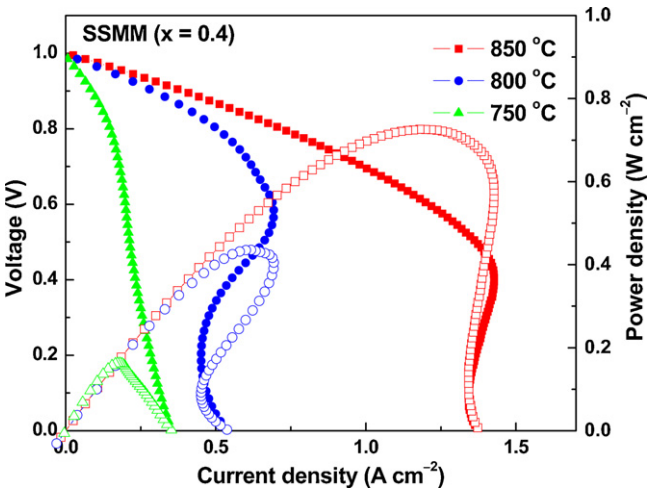

Fig. 6. Cell voltage and power density of a SBCO/LSGM/SDC/SSMM ($x = 0.4$) cell as a function of current density measured at 700–850 °C using wet commercial city gas as the fuel and ambient air as the oxidant.

As an excellent SOFC anode operating in hydrocarbons containing H_2S fuel, it must possess good carbon and sulfur tolerance and high electrocatalytic activity. Fig. 6 shows the typical cell voltage and power density of a SBCO/LSGM/SDC/SSMM ($x = 0.4$) cell as a function of current density obtained using wet commercial city gas containing H_2S as fuel in the temperature range of 750–850 °C. The wet commercial city gas (3% H_2O) contains around 5 ppm H_2S and complex hydrocarbons, as described in Ref. [41]. Fig. 6 shows that the maximum power density in commercial city gas containing H_2S reaches 726, 435, and 163 mW cm^{-2} at 850, 800, and 750 °C, respectively. The *I–V* curves are non-linear and show sharply negative curvatures, and the current density is limited to the relatively high current density region, which is often observed in direct hydrocarbon SOFCs [42,43]. However, no such obvious phenomena occur in the high current density region with H_2 as the fuel (Fig. 5(c)).

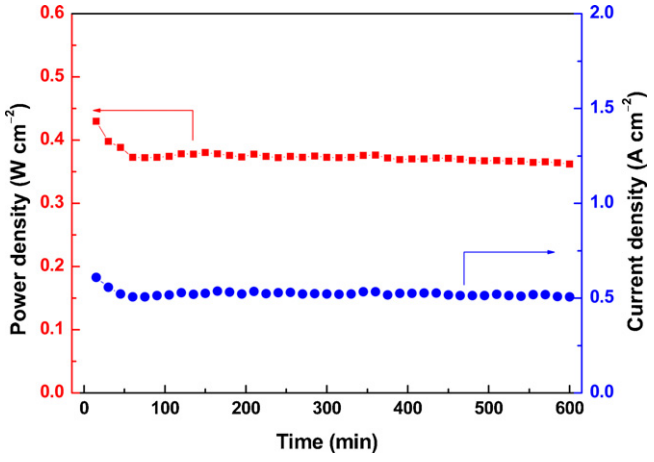

Fig. 7. Power density and corresponding current density of a single cell with an SSMM ($x = 0.4$) anode as a function of time operated in wet commercial city gas at 850 °C.

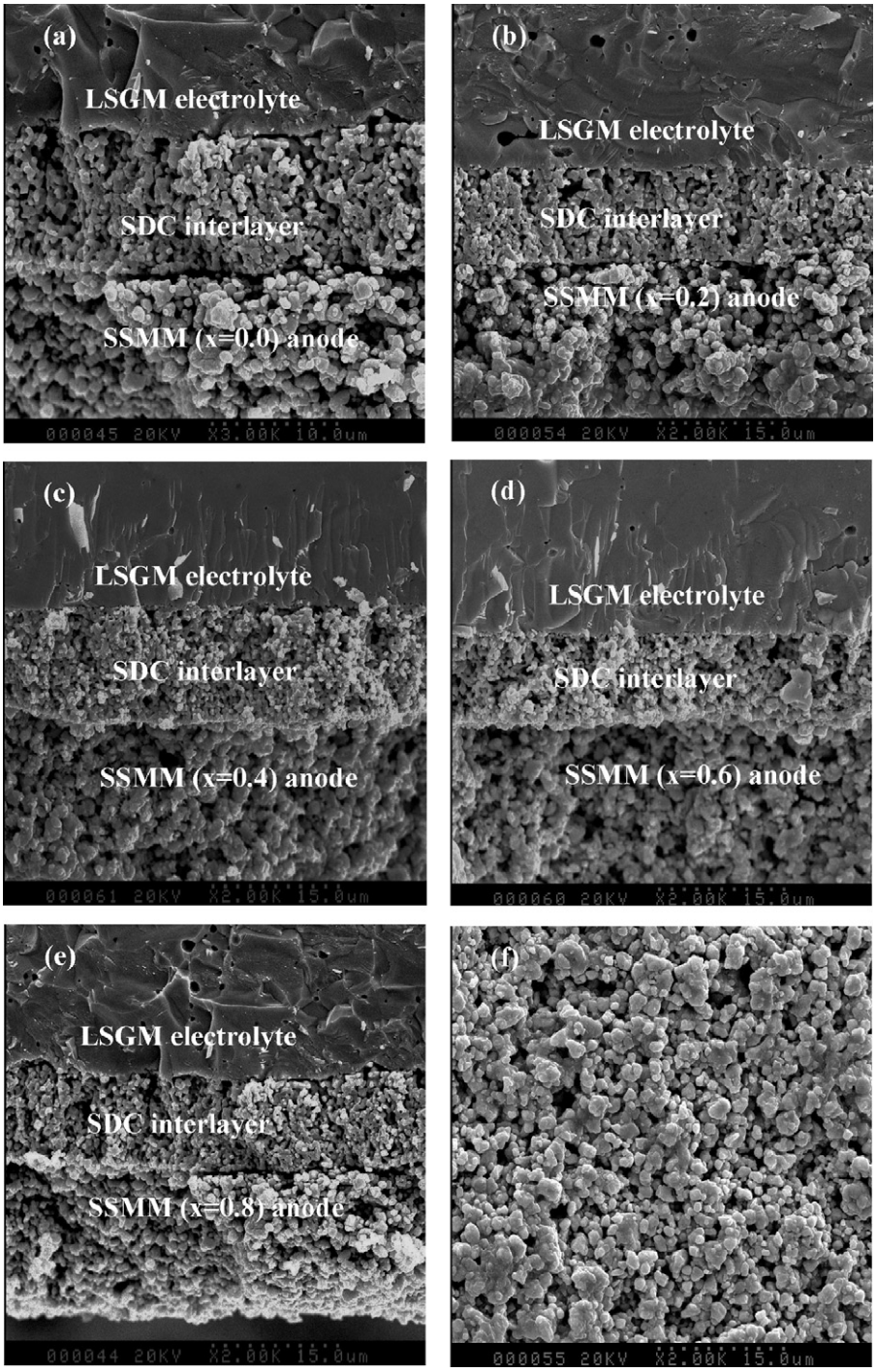

Fig. 8. SEM micrographs of the anode/electrolyte interface after cell testing. (a) $x = 0.0$. (b) $x = 0.2$. (c) $x = 0.4$. (d) $x = 0.6$ (e) $x = 0.8$. (f) Surface of the SSMM ($x = 0.4$) anode after operating in city gas. The anodes on the interlayer were sintered at 950 °C for 2 h in a nitrogen atmosphere.

This is mainly because the catalytic activity of SSMM ($x = 0.4$) is lower for the oxidation of hydrocarbons than that for the oxidation of hydrogen [43]. To assess the electrochemical stability of the SSMM ($x = 0.4$) anode in complex hydrocarbons, the cell was operated in city gas containing H_2S at 800 °C for 10 h. Fig. 7 shows the electrochemical stability test curve of the SBCO/LSGM/SDC/SSMM ($x = 0.4$) cell. The maximum power density declines from 435 to 373 mW cm^{-2} during the first 45 min of operation. The initial decrease in the power density of the cell in city gas is mainly due to the fuel-switch control from H_2 to city gas to achieve a new equilibrium in the system. The cell power density, which decreases from 373 to 363 mW cm^{-2} over the remaining time of operation, represents only a degradation of only 2.68%, implying that the SSMM ($x = 0.4$) anode is relatively stable. No carbon deposition is observed on the anode surface after cell testing, which is further confirmed by SEM observations (Fig. 8(f)). As discussed above, the SSMM with $x = 0.4$ anode exhibits excellent electrochemical performance and good stability in city gas containing H_2S, indicating that this anode functions well with both carbon and sulfur in commercial city gas containing H_2S.

To inspect the microstructure of the cell after testing, SEM was used to observe the cross-section of the cell and the anode sur-

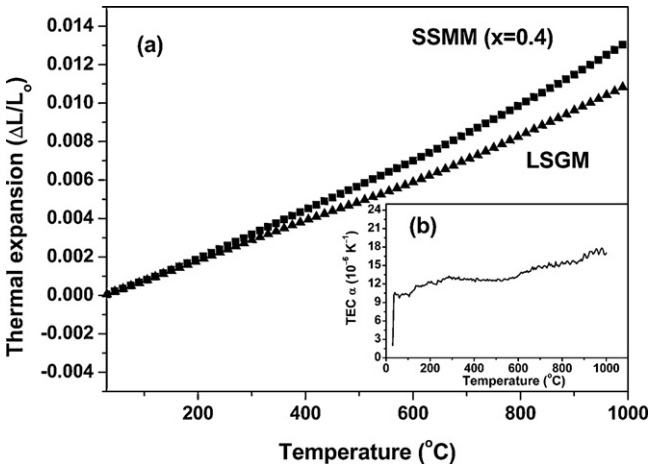

Fig. 9. (a) Thermal expansion and (b) TEC curves of the SSMM sample ($x = 0.4$) between 30 and 1000 °C in a nitrogen atmosphere.

face. Fig. 8 shows the SEM micrographs of the anode/electrolyte interface and the surface of the SSMM anodes ($0 \le x \le 0.8$). The electrolyte is highly dense besides small closed pores observed. An interlayer approximately 10 μm-thick is clearly visible between the SSMM anodes and the LSGM electrolytes. No delamination of the anodes from the interlayer is observed in the SEM micrographs. However, careful observations show an interfacial gap between the SSMM anode and the SDC interlayer of samples with $x = 0.00$, 0.02, and 0.08, whereas good bonding and continuous contact at the anode/interlayer interface are observed in samples with $x = 0.04$ and 0.06, indicating good thermal-expansion compatibility between the two materials. Fig. 8(f) shows the SEM micrograph of the SSMM ($x = 0.4$) anode surface after operating in city gas. The SSMM ($x = 0.4$) anode shows a homogeneous distribution of pores and particles with grain sizes ranging from 1 to 3 μm. No carbon deposition is observed on the surface of the SSMM ($x = 0.4$) anode, indicating good carbon tolerance.

3.4. Thermal-expansion behavior

As SOFCs operate at high temperatures and should be able to endure the thermal cycle from room temperature to operating temperature, the electrode materials must be thermally compatible with the other cell components [44]. The thermal-expansion behavior of the selected SSMM ($x = 0.4$) sample was measured for its high-phase purity, good conductivity, and electrochemical performance as a potential anode material. Fig. 9(a) shows the thermal-expansion curves of the SSMM sample with $x = 0.4$ and LSGM over the temperature range of 30–1000 °C in a nitrogen atmosphere. The thermal-expansion curve of the SSMM ($x = 0.4$) is almost linear. The average TEC value is $13.5 \times 10^{-6}\ K^{-1}$ in the temperature range of 30–1000 °C, close to that of the LSGM electrolyte under the same condition ($11.2 \times 10^{-6}\ K^{-1}$) and indicating that the SSMM anode ($x = 0.4$) has good thermal-expansion compatibility with the LSGM electrolyte. This agrees well with the SEM observations. To identify the volume change in the SSMM anode ($x = 0.4$) in a nitrogen atmosphere, the TEC curve is shown in Fig. 9(b). No abrupt changes occur in the TEC curve, suggesting that there is no structural transition in the measured temperature range.

4. Conclusions

Double-perovskite SSMM ($0 \le x \le 0.8$) was synthesized by a sol–gel technique for assessment as a possible anode material for SOFCs with LSGM electrolytes. The impurities began to appear in double-perovskite SSMM when $x \ge 0.6$, and the contents of the impurities increased with increasing Sm contents. As x increased from 0.0 to 0.8, the ordering of the Mg/Mo ions at the B/B′ sites decreased. The electrical conductivity of the SSMM samples significantly increased with the substitution of Sm for Sr. The highest conductivity was achieved by the $x = 0.6$ sample, which reached a maximum of 16 S cm^{-1} in H_2 at 800 °C. The single-cell that used the SSMM ($x = 0.6$) anode achieved a maximum power-density of 907 mW cm^{-2} at 850 °C. These results indicated that substitution of Sm for Sr in SSMM double-perovskites clearly increases the amount of the Mo^{5+}/Mo^{6+} redox couple and, hence, the electrical conductivity and electrochemical performance (Mo has good catalysis). However, impurities appeared in the sample with $x = 0.6$, although its performance was nevertheless excellent. The double-perovskite SSMM with $x = 0.4$ may be recommended as a good anode candidate in view of its overall performance. The SSMM with $x = 0.4$ anode was stable at 1100 °C under a nitrogen atmosphere. The TEC of the SSMM with $x = 0.4$ anode was $13.5 \times 10^{-6}\ K^{-1}$ in the nitrogen atmosphere, close to that of the LSGM electrolyte and indicating good thermal-expansion compatibility. The SSMM with $x = 0.4$ anode displayed excellent electrochemical performance and stability in the commercial city gas containing H_2S. Preliminary results indicated that this anode had good carbon and sulfur tolerance in commercial city gas containing H_2S.

Acknowledgements

This work was supported by the Natural Science Foundation of China under Contract No. 10974065 and the Scientific Research Foundation for the Returned Overseas Chinese Scholars, State Education Ministry.

References

[1] B.C.H. Steele, A. Heinzel, Nature 414 (2001) 345–352.
[2] E.P. Murray, T. Tsai, S.A. Barnett, Nature 400 (1999) 649–651.
[3] S. Park, J.M. Vohs, R.J. Gorte, Nature 404 (2000) 265–267.
[4] S. McIntosh, R.J. Gorte, Chem. Rev. 104 (2004) 4845–4865.
[5] S.P. Jiang, S.H. Chan, J. Mater. Sci. 39 (2004) 4405–4439.
[6] S. Tao, J.T.S. Irvine, Nat. Mater. 2 (2003) 320–323.
[7] A. Atkinson, S. Barnett, R.J. Gorte, J.T.S. Irvine, A.J. McEvoy, M. Mogensen, S.C. Singhal, J. Vohs, Nat. Mater. 3 (2004) 17–27.
[8] J.B. Goodenough, Y.H. Huang, J. Power Sources 173 (2007) 1–10.
[9] B.C.H. Steele, I. Kelly, H. Middleton, R. Rudkin, Solid State Ionics 28–30 (1988) 1547–1552.
[10] O.A. Marina, N.L. Canfield, J.W. Stevenson, Solis State Ionics 149 (2002) 1–2.
[11] Q.X. Fu, F. Tietz, Fuel Cell 8 (2008) 283–293.
[12] J. Peña-Martínez, D. Marrero-López, J.C. Ruiz-Morales, C. Savaniu, P. Núñez, J.T.S. Irvine, Chem. Mater. 18 (2006) 1001–1006.
[13] E.S. Raj, J.T.S. Irvine, Solid State Ionics 180 (2010) 1683–1689.
[14] J.C. Ruiz-Morales, J. Canales-Vázquez, C. Savaniu, D. Marrero-López, W. Zhou, J.T.S. Irvine, Nature 439 (2006) 568–571.
[15] M.J. Escudero, J.T.S. Irvine, L. Daza, J. Power Sources 192 (2009) 43–50.
[16] M.C. Zhan, W.D. Wang, T.F. Tian, C.S. Chen, Energy Fuels 24 (2010) 764–771.
[17] N. Danilovic, J.L. Luo, K.T. Chuang, A.R. Sanger, J. Power Sources 192 (2009) 247–257.
[18] A. Aguadero, C. de la Calle, J.A. Alonso, D. Pérez-Coll, M.J. Escudero, L. Daza, J. Power Sources 192 (2009) 78–83.
[19] G.L. Xiao, Q. Liu, X.H. Dong, K. Huang, F.L. Chen, J. Power Sources 195 (2010) 8071–8074.
[20] S.W. Tao, J.T.S. Irvine, J. Electrochem. Soc. 151 (2004) A252–A259.
[21] S. Zha, P. Tsang, Z. Cheng, M. Liu, J. Solid State Chem. 178 (2005) 1844–1850.
[22] Y.H. Huang, R.I. Dass, Z.L. Xing, J.B. Goodenough, Science 312 (2006) 254–257.
[23] Y.H. Huang, R.I. Dass, J.C. Denyszyn, J.B. Goodenough, J. Electrochem. Soc. 153 (2006) A1266–A1272.
[24] Y. Matsuda, M. Karppinen, Y. Yamazaki, H. Yamauchi, J. Solid State Chem. 182 (2009) 1713–1716.
[25] Y. Ji, Y.H. Huang, J.R. Ying, J.B. Goodenough, Electrochem. Commun. 9 (2007) 1881–1885.
[26] D. Marrero-López, J. Peña-Martinez, J.C. Ruiz-Morales, M.C. Martin-Sedeño, P. Núñez, J. Solid State Chem. 182 (2009) 1027–1034.
[27] D. Marrero-López, J. Peña-Martínez, J.C. Ruiz-Morales, D. Pérez-Coll, M.A.G. Aranda, P. Núñez, Mater. Res. Bull. 43 (2008) 2441–2450.
[28] C. Bernuy-Lopez, M. Allix, C.A. Bridges, J.B. Claridge, M.J. Rosseinsky, Chem. Mater. 19 (2007) 1035–1043.

[29] Q.J. Zhou, T.M. He, Y. Ji, J. Power Sources 185 (2008) 754–758.
[30] L.G. Cong, T.M. He, Y. Ji, P.F. Guan, Y.L. Huang, W.H. Su, J. Alloys Compd. 348 (2003) 325–331.
[31] J.F. Xue, Y. Shen, Q.J. Zhou, T.M. He, Y.H. Han, Int. J. Hydrogen Energy 35 (2010) 294–300.
[32] F. Wang, Q.J. Zhou, T.M. He, G.D. Li, H. Ding, J. Power Sources 195 (2010) 3772–3778.
[33] D. Marrero-López, J. Peña-Martínez, J.C. Ruiz-Morales, M. Gabás, P. Núñez, M.A.G. Aranda, J.R. Ramos-Barrado, Solid State Ionics 180 (2010) 1672–1682.
[34] L.C. Kong, B.W. Liu, J. Zhao, Y.S. Gu, Y. Zhang, J. Power Sources 188 (2009) 114–117.
[35] R. Ratheesh, M. Wöhlecke, B. Berge, Th. Wahlbrink, H. Haeuseler, E. Rühl, R. Blachnik, P. Balan, N. Santha, M.T. Sebastian, J. Appl. Phys. 88 (2000) 2813–2818.
[36] N. Setter, I. Laulicht, Appl. Spectrosc. 41 (1987) 526–528.
[37] L.I. Balcells, J. Navarro, M. Bibes, A. Roig, B. Martínez, J. Fontcuberta, Appl. Phys. Lett. 78 (2001) 781–783.
[38] M. García-Hernández, J.L. Martínez, M.J. Martínez-Lope, M.T. Casais, J.A. Alonso, Phys. Rev. Lett. 86 (2001) 2443–2446.
[39] R.D. Shannon, Acta Crystallogr. A32 (1976) 751–767.
[40] S.P.S. Porto, J.F. Scott, Phys. Rev. 157 (1967) 716–719.
[41] L.L. Zhang, Q.J. Zhou, T.M. He, J. Power Sources 195 (2010) 6356–6366.
[42] Y.B. Lin, Z.L. Zhan, J. Liu, S.A. Barnett, Solid State Ionics 176 (2005) 1827–1835.
[43] X.B. Zhu, Z. Lü, B. Wei, K.F. Chen, M.L. Liu, J. Power Sources 190 (2009) 326–330.
[44] M. Mori, N.M. Sammes, Solid State Ionics 146 (2002) 301–312.